AGU ADVANCING EARTH AND SPACE SCIENCE

Geophysical Research Letters

RESEARCH LETTER
10.1029/2021GL093013

The First Detection of an Earthquake From a Balloon Using Its Acoustic Signature

Quentin Brissaud[1,2], Siddharth Krishnamoorthy[3], Jennifer M. Jackson[1], Daniel C. Bowman[4], Attila Komjathy[3], James A. Cutts[3], Zhongwen Zhan[1], Michael T. Pauken[3], Jacob S. Izraelevitz[3], and Gerald J. Walsh[3]

[1]Seismological Laboratory, California Institute of Technology, Pasadena, CA, USA, [2]the Norwegian Seismic Array (NORSAR), Oslo, Norway, [3]Jet Propulsion Laboratory, California Institute of Technology, Pasadena, CA, USA, [4]Sandia National Laboratories, Albuquerque, NM, USA

Key Points:

- First detection of a natural earthquake using balloon-borne infrasound data
- Rayleigh wave-induced infrasound dispersion characteristics provide constraints on subsurface velocities
- Shallow waveguides, focal mechanism, and subwavelength topographic changes control infrasound amplitude and dispersion by weak earthquakes

Supporting Information:

Supporting Information may be found in the online version of this article.

Correspondence to:

S. Krishnamoorthy, siddharth.krishnamoorthy@jpl.nasa.gov

Citation:

Brissaud, Q., Krishnamoorthy, S., Jackson, J. M., Bowman, D. C., Komjathy, A., Cutts, J. A., et al. (2021). The first detection of an earthquake from a balloon using its acoustic signature. *Geophysical Research Letters*, *48*, e2021GL093013. https://doi.org/10.1029/2021GL093013

Received 16 FEB 2021
Accepted 23 APR 2021

Abstract Extreme temperature and pressure conditions on the surface of Venus present formidable technological challenges against performing ground-based seismology. Efficient coupling between the Venusian atmosphere and the solid planet theoretically allows the study of seismically generated acoustic waves using balloons in the upper atmosphere, where conditions are far more clement. However, earthquake detection from a balloon has never been demonstrated. We present the first detection of an earthquake from a balloon-borne microbarometer near Ridgecrest, CA in July 2019 and include a detailed analysis of the dependence of seismic infrasound, as measured from a balloon on earthquake source parameters, topography, and crustal and atmospheric structure. Our comprehensive analysis of seismo-acoustic phenomenology demonstrates that seismic activity is detectable from a high-altitude platform on Earth, and that Rayleigh wave-induced infrasound can be used to constrain subsurface velocities, paving the way for the detection and characterization of such signals on Venus.

Plain Language Summary The interior structure of Venus remains unknown due to lack of in situ seismic observations. Adverse temperature and pressure conditions on the Venusian surface limit the lifetimes of landers to a few hours, which poses a technological challenge against performing ground-based seismology to detect venusquakes. Seismic energy on Venus, as on Earth, can be transmitted into the atmosphere through mechanical coupling and propagate as low-frequency sound (infrasound). Infrasound from earthquakes travels long distances and has been detected from ground-based stations. This mechanism may allow the detection of seismically generated pressure disturbances on Venus using balloons, enabling remote seismology from its upper atmosphere, where temperature and pressure conditions are far more clement and longer mission lifetimes are likely. However, the feasibility of such a technique has yet to be established through the detection of ground motion following an earthquake using a freely floating balloon. We demonstrate the first detection of an earthquake from a high-altitude balloon. We explore the dependence of the pressure signal seen by the balloon on parameters such as the magnitude, focal mechanism, location of the earthquake, surface topography, and atmospheric structure. We also show how the signal recorded at the balloon can be used to study the subsurface.

1. Introduction

The surface of Venus hosts several volcanic structures and displays clear signs of tectonic strain (Byrne et al., 2018). However, whether the planet is presently experiencing volcanic eruptions and venusquakes is presently unknown. Several geophysical studies involving simulations and analysis of data from orbiter missions have suggested that the planet may currently be geologically active (e.g., Esposito, 1984; Filiberto et al., 2020; Gülcher et al., 2020; Lognonné & Johnson, 2015; Smrekar et al., 2010). With temperature greater than 460°C and pressure near 90 atmospheres (Wood et al., 1968) at the Venusian surface, no lander has survived longer than 3 h, which is much too short for quantifying the levels of present-day seismic activity. Landers that can operate on the surface of Venus for 60 Earth days or more are being developed (Kremic & Hunter, 2019), but technical challenges owing to the harsh environment render sensitive seismometers infeasible in initial missions, and perhaps even for an extended period of time beyond. Atmospheric conditions at altitudes of 50–60 km on Venus are far more clement (Linkin et al., 1986) and longer sensor lifetimes are likely, evidenced by >40-h flights of the Soviet Vega balloons in 1985 (Sagdeev et al., 1986). Recent

NASA-sponsored studies suggest that lifetimes of over 60 Earth days are achievable (Cutts et al., 2018; Gilmore & Beauchamp, 2020). This implies that seismic monitoring, if it could be performed from a balloon platform, may be able to circumvent the severe limitations on mission lifetime on the surface.

Seismic energy excites infrasound, that is, low-frequency acoustic waves (<20 Hz, below the limit of human hearing), through seismo-acoustic coupling at the solid planet-atmosphere interface. These waves encode information about the seismic source and the internal structure (Garcia et al., 2005). Infrasound waves from earthquakes and volcanic eruptions have been detected by ground-based monitoring stations, routinely. Ground-based recordings have helped advance understanding of the physical mechanism, through which infrasound is generated near the epicenters of earthquakes (e.g., Arrowsmith et al., 2012; Johnson et al., 2020; Shani-Kadmiel et al., 2021), while acoustic recordings in the vicinity of volcanoes can offer insight into preeruptive and coeruptive seismicity and outgassing (Fee & Matoza, 2013; Kanamori & Mori, 1992; Lamb et al., 2017).

Balloon-based infrasound monitoring was initially developed for military use (Banister & Hereford, 1991; Peebles, 1997) but has also found applications in geophysics. For example, Wescott (1965) studied turbulent structures in the atmosphere using balloon-borne microphones, Matoza et al. (2017) were able to characterize the acoustic wavefield of Strombolian eruptions in the vertical direction using tethered balloons, Bowman and Lees (2017) investigated ocean microbarom sources using infrasound, and Lamb et al. (2018) retrieved the acoustic signature of thunderstorms in low-frequency acoustic records. On Venus, seismo-acoustic coupling is over 60 times stronger than on Earth (Garcia et al., 2005). Thus, studying acoustic waves generated through seismo-acoustic coupling using balloon and orbiter-based (see Didion et al., 2018) implementations may be an effective way to determine current levels of seismicity and volcanism (Stevenson et al., 2015).

Development work on a balloon-based infrasound detection technique has thus far focused primarily on the short-range detectability of infrasound produced by weak seismic signals, generated with controlled artificial sources such as a "seismic hammer" (Krishnamoorthy et al., 2018, 2019; Martire et al., 2018) and subsurface chemical explosions (Garcia et al., 2020), in a concerted effort to use Earth-based experiments as an analog for Venus. However, a natural earthquake has not been observed from a balloon platform yet. Experiments utilizing artificial seismic sources are crucial to establish the existence of airborne seismo-acoustic signals, but lack the scientific complexities introduced by the interaction of seismic waves with the Earth's interior structure and composition, the extensive effects of Earth's atmospheric structure (i.e., path effects), and the operational complexities of an uncontrolled balloon-based seismology experiment. A platform moving within the atmosphere introduces additional complexities to the process of retrieving geophysical information from an infrasound pressure trace. Success in such an effort requires a multipronged approach, combining multiple streams of data with model-based studies of seismo-acoustic signal generation and propagation on Earth and on Venus (Garcia et al., 2005; Trahan & Petculescu, 2020).

We report for the first time the detection of a natural earthquake from a freely floating balloon platform using a combination of experimental data and simulation. We present a detailed analysis of the role that the earthquake's properties such as depth and faulting mechanism, the Earth's crustal structure, topography, and atmospheric conditions play on the generation, propagation, and detectability of seismic infrasound signals from a balloon. Finally, we comment on the information that can be gleaned about crustal structure of the planet from characterizing the infrasound signal on a balloon.

2. The Ridgecrest Balloon Experiment

The two main shocks of the 2019 Ridgecrest earthquake sequence with magnitudes M_w 6.4 and 7.1 occurred on July 4 and July 7, 2019 (1833 and 0419 UTC), respectively. A lengthy aftershock sequence followed, which saw the occurrence of over 10,000 earthquakes of $M_w \geq 1.5$ over the next 6 weeks, primarily in the Owens valley region of California (Ross et al., 2019). As part of a rapid response campaign, we manufactured, tested, and launched four "Heliotrope" (Bowman et al., 2020) solar-heated stratospheric balloons equipped with high-altitude sensor packages. Two of these balloons with a 6 m diameter envelope were launched on July 22, 2019 from Johnson Valley, CA and carried one sensor package each, equipped with a Paroscientific Digiquartz 6000-15A-IS microbarometer and an InertialSense μINS inertial measurement

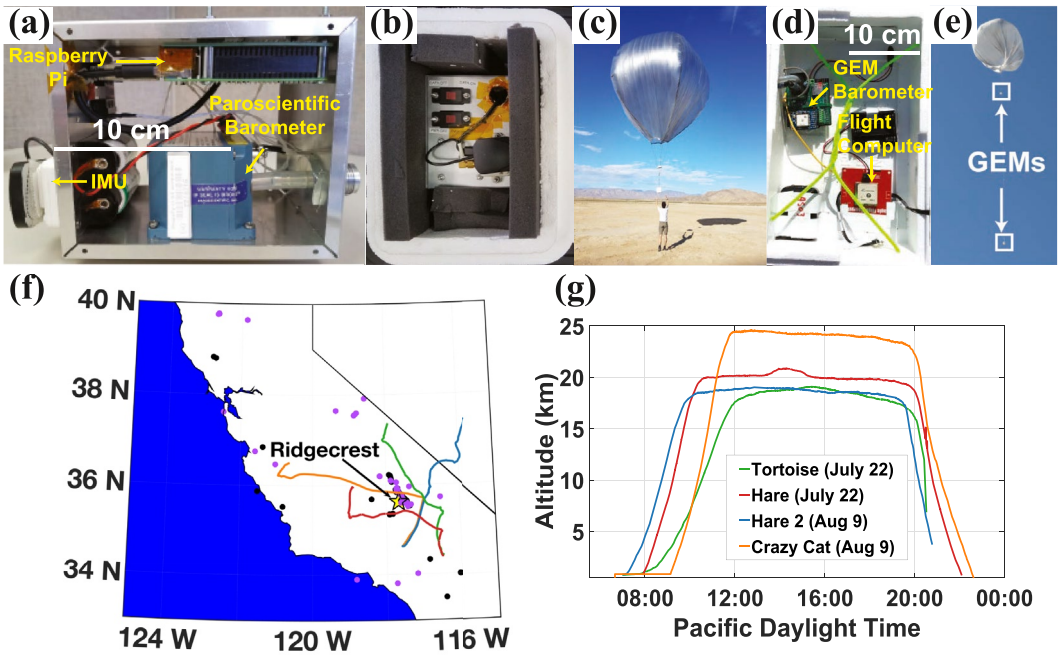

Figure 1. The Ridgecrest balloon experimental campaign. (a) Sensor package for Tortoise, Hare, and Hare 2 balloons, "IMU" stands for Inertial Measurement Unit (b) Sensor packaged for flight, (c) Launch of the Hare balloon, (d) Sensor package for the CrazyCat balloon, (e) CrazyCat balloon with two sensor packages on a 36-m tether, (f) and (g), The trajectory and altitude profile of the balloons. Hare and Tortoise balloons flew on July 22, 2019, whereas Hare 2 and CrazyCat flew on August 9, 2019. Earthquakes with $M_w \geq 1.5$ occurring during the July 22 campaign are shown as black dots, and those on August 9 are shown as magenta dots. Stratospheric wind velocities exhibited strong altitude dependence on these days, leading to the divergence in trajectories of balloons launched from the same location.

unit (IMU), with measurements coordinated using a Raspberry Pi 3B single-board computer. The construction of this sensor package with its components is shown in Figure 1a, with its packaging for flight and launch shown in Figures 1b and 1c, respectively. The IMU was used to track the location and motion of the sensor package as the balloon floated with the prevailing wind. Since infrasound waves have wavelengths that are much larger than the size of our sensor package, the orientation of the package does not affect the amplitude of the arrival.

Balloons flown on July 22, 2019, nicknamed "Tortoise" and "Hare," ascended to float altitudes of 19 and 20 km, respectively. While each balloon floated for nearly 10 h before self-terminating at sunset, thermal anomalies caused power failure on the sensor packages after ~5 h. Two additional balloons were launched from El Mirage, CA on August 9, 2019. One balloon, a 6 m diameter envelope, nicknamed "Hare 2," contained a package identical to that of Hare and reached a float altitude of ~18 km. The second balloon, a 10 m diameter envelope with larger lift capacity nicknamed "CrazyCat," carried two GEM (Anderson et al., 2018) microbarometers on a 36 m long tether with a High-Altitude Science Eagle Flight Computer for position tracking (see Figures 1d and 1e) and reached a float altitude of 24 km. On this occasion, all sensor packages lasted the duration of the flight. All four balloons and their payloads were successfully recovered. Figures 1f and 1g show the trajectory of the four balloons and the earthquakes with $M_w \geq 1.5$ that occurred during the flights.

3. Earthquakes on July 22 and August 9, 2019

Earthquakes that occurred on July 22 and August 9, 2019 are dominated by a strong strike-slip component with very few events showing large normal or reverse components (see supplementary Section S2). Strike-slip-dominated events generally lead to small vertical ground motion and produce lower infrasound amplitudes through ground-air coupling than normal or reverse faults of the same magnitude. Such variations in infrasound amplitudes with changes in fault orientations have been observed in the ionosphere

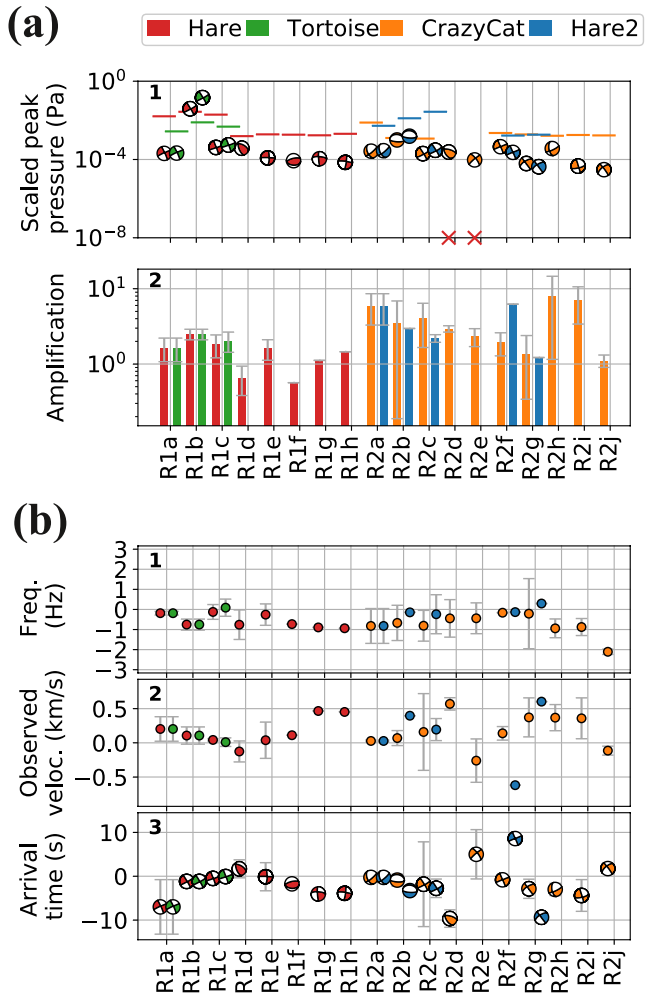

Figure 2. Selection of Rayleigh wave infrasound events from their predicted signal-to-noise ratio (SNR). (*a*1) Simulated peak pressure (Pa) at the balloon, listed in supplementary Table S1, multiplied by the amplification factor presented in the panel. Peak amplitudes are represented by the beachballs of each focal mechanism with colors corresponding to each balloon. Horizontal lines correspond to the noise level computed from the average value of the detrended Welch spectrum between 0.3 and 5 Hz in a 50 s window surrounding the time of each event. Event R1b is the only event with scaled peak pressure larger than the noise level. Red crosses indicate events for which the signal is polluted by the large-amplitude spurious noise. (*a*2) Peak vertical velocity ratio between seismic data $\tilde{v}_{z,data}$ over simulated signals $\tilde{v}_{z,simu}$ such that $A_{vz} = \tilde{v}_{z,data} / \tilde{v}_{z,simu}$. The amplification is an average from the closest regional seismic stations to the balloon horizontal location (within 30 km from the balloon) at the time of the event. The corresponding standard deviation is shown as gray error bars around each bar. (b) Differences between data and the simulation for each event for (b1) dominant frequencies, (b2) observed velocities, and (b3) arrival times. Standard deviations of the differences are shown as gray error bars around each beachball. Observed arrival times and dominant frequencies (panels b1, b2, b3) are computed from the frequency and time at peak amplitude in the spectrogram associated with the arrival recorded at each seismic station (see supplementary Section S4.2).

(Perevalova et al., 2014). With low expected signal-to-noise ratio (SNR), pressure records at the balloons require careful investigation to confirm the presence of seismically induced infrasound arrivals, since spurious noise could generate arrivals that appear to be of seismic origin (Krishnamoorthy et al., 2020). The acoustic wavefield in the atmosphere excited by an earthquake includes both epicentral (generated by ground motion at the epicenter) and Rayleigh wave-induced (generated by seismic waves as they traverse the crust) infrasound phases (see supplementary Section S3). To prioritize seismic events and streamline the investigation of pressure signals, we adopt a four-step procedure (see supplementary Section S1.3) that consists of shortlisting events by numerical modeling (acoustic ray-tracing using the GeoAc package described in Blom & Waxler, 2012 and Green's function methods using "RW-atmos") of the arrival time and amplitude of each phase type (see supplementary Section S7).

In the absence of strong inhomogeneous seismic wave coupling, high-frequency epicentral infrasound excited by small earthquakes is transmitted to the atmosphere along steep propagation angles (see supplementary Figure S7). With the tropospheric jet blowing northward on July 22 and August 9, balloons were generally located in the acoustic shadow zone within 150 km from the source at altitudes <25 km (see supplementary Section S4). While topographic diffraction and small-scale wind heterogeneities allow acoustic energy to leak into the shadow zone (Chunchuzov et al., 2015; Hernandez et al., 2018), the waveform investigation of each likely arrival (see supplementary Section S4) did not lead to any epicentral detection during our flights. Unscaled simulated Rayleigh waves show small pressure perturbations at the balloons for most events, with amplitudes comparable to or lower than the recorded pressure noise level (see supplementary Section S1.3 and Figure S2). At high frequency, seismic amplitudes are sensitive to the rapid variations of shear velocities in the shallow crust (<2 km depth), which are poorly constrained in available tomographic models (Berg et al., 2018). Events with the largest Rayleigh wave infrasound amplitudes were, therefore, scaled using surface seismic velocities to account for site effects (see supplementary Section S1.3).

Figure 2a shows that while most events do not have large SNR, our model predicts a strong arrival for a M_w 4.2 event that occurred during the ascent of both Tortoise and Hare balloons (event "R1b," Figure 2). Event R1b is the only event exhibiting scaled expected peak pressure of 0.14 Pa, larger than the noise level, with SNR of 2.5 (see also Figure 3d). The surface wave origin of this arrival is confirmed by the error amplitudes shown in Figure 2b, indicating that the model captures the arrival time and amplitude of the seismic wave train with an error <4 s in arrival time and 1 Hz in frequency. Larger discrepancies occur either when there is no clear arrival at the seismic station (e.g., event R1a; see supplementary Section S4) due to the absence of three-dimensional path effects, that is, heterogeneity in the distribution of low-velocity material in the region or high uncertainty in the moment tensor solutions. Semianalytical computations provide a first estimate of the expected seismically generated acoustic wavefield. However, they neglect body wave phases and lateral variations of shear velocity and topography. While basin and topographic effects on seismo-acoustic coupling have been estimated at ground stations for large earthquakes (Hernandez et al., 2018) and for small earthquakes (M_w 3.6) at short distance from the source (Johnson et al., 2020),

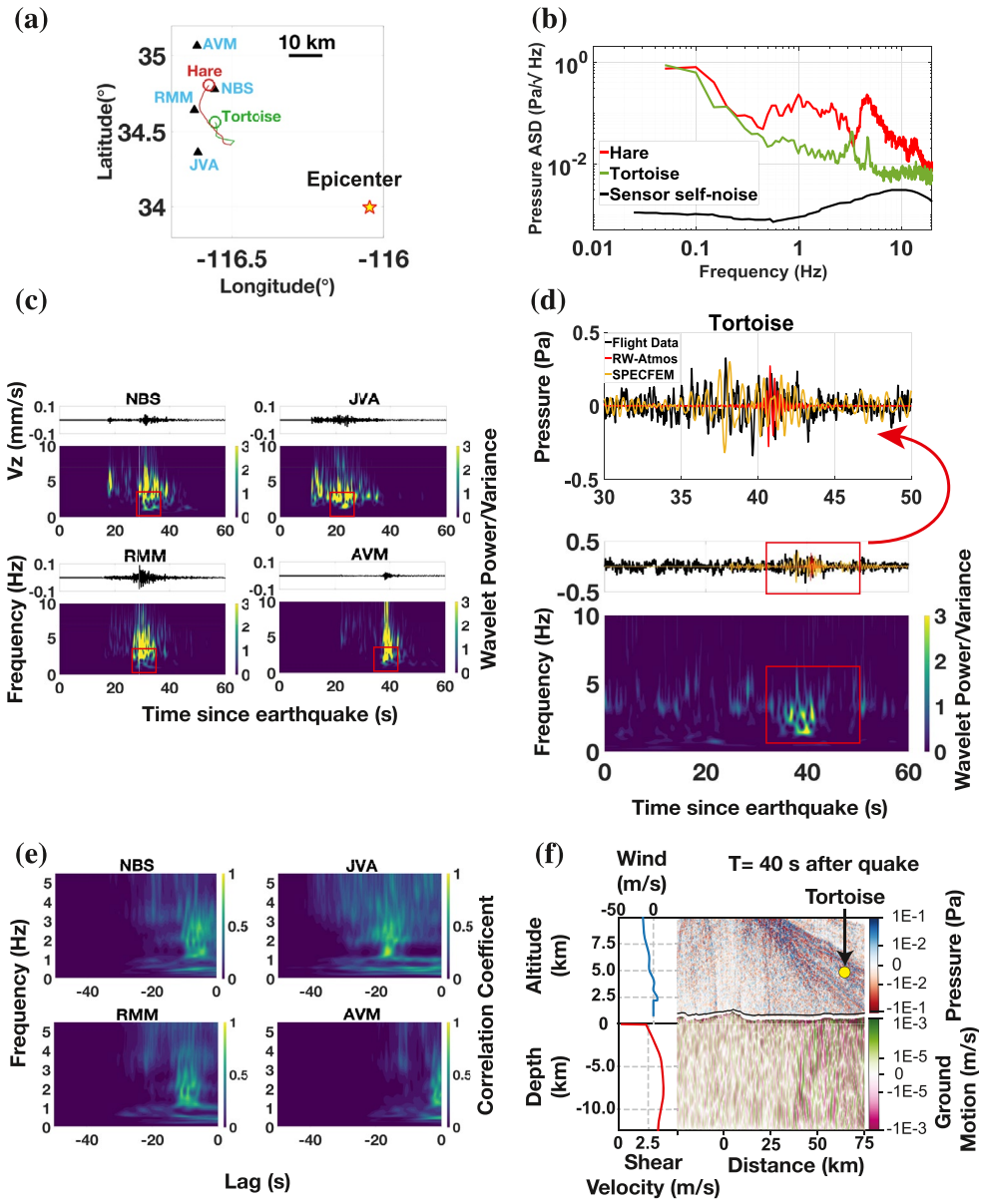

Figure 3. The first detection of an earthquake from a balloon. (a) Location of the balloons (circles), seismic stations (triangles) and the epicenter of event R1b (star) extracted from the SCEC seismic catalog (see supplementary Section S1.1), (b) Background pressure noise levels experienced by Hare and Tortoise microbarometers. The noise level is shown as the amplitude spectral density (ASD) with unit $Pa / \sqrt{Hz}$. Hare experienced a higher noise background due to faster ascent, especially in the 1–10 Hz band. Peaks at >3 Hz in the frequency spectrum are caused by vortex shedding from the envelope; they appear as quasiperiodic bursts of energy in spectrograms and disappear once the balloons reach float. (c) Cluster of plots showing time series and wavelet spectrograms for four seismic stations near the Tortoise balloon, (d) Time series recorded by the Tortoise microbarometer compared with RW-Atmos and SPECFEM-DG simulations, with the inset magnified to show agreement between simulated and recorded data. Simulated waveforms were scaled down by a factor of 4,000 to account for geometrical spreading, then scaled up by a factor of 2.72, after comparison with ground motion data from the nearest seismic station (RMM) to compensate for local site effects (see supplementary Section S5). (e) Two-dimensional time-frequency correlations between the spectrograms of the seismic stations and the Tortoise microbarometer show high correlation in the 1–3 Hz band, with lag consistent with the travel time for a signal from the ground to the balloon's altitude of ~4.8 km. (f) A snapshot of the SPECFEM-DG simulation showing the propagation of the seismic wave along the Earth's crust and the arrival of infrasound at Tortoise, with the same scaling as in panel (d).

the complex interplay between the source mechanism, shallow shear velocities, and topographic structures remains poorly constrained and requires accurate modeling. All of the other events presented in Figure 2 have also been individually investigated, but we could not certify detections with certainty for events apart from R1b (see supplementary Section S4).

3.1. Earthquake Detection

Semianalytical results indicate a strong arrival at both Tortoise and Hare 42 s after event R1b on July 22, the only event with expected peak pressure larger than the noise level. Both balloons were located 78 km from the epicenter at the time of event (Figure 3a). Figure 3c shows the time series and corresponding spectrograms at each station confirming the presence of large seismic wave arrivals at 38 s between 1 and 3 Hz at Tortoise (Figure 3d), indicating a possible Rayleigh wave-induced arrival. The pressure spectrogram shows a strong correlation to the seismic velocity spectrograms at the ground between 1 and 3 Hz, further supporting the detection of Rayleigh wave-induced infrasound (Figure 3e). The cross-correlation time lags are consistent with the horizontal seismic propagation time between Tortoise and each of the stations (Figure 3c), followed by the travel time of acoustic waves in the air. Additionally, the strong cross-correlation between 1 and 3 Hz, in Figure 3e, highlights the absence of significant acoustic wave dispersion in the atmosphere typical of infrasound propagating at regional distances (Bass et al., 2007). The acoustic energy at frequencies between 3 and 5 Hz does not exhibit large SNR owing to the presence of strong vortex shedding at the balloon in this frequency band (see Figure 3b).

To further confirm the seismo-acoustic arrival, we ran a full-waveform simulation of coupled seismo-acoustic waves including topography and attenuation for event R1b using SPECFEM2D-DG (Figure 3f, see also supplementary Section S5), a high-fidelity seismo-acoustic simulation package (Brissaud et al., 2017). A clear quasiplanar acoustic wavetrain is visible traveling through Tortoise's location, corresponding to the arrival observed in the pressure records in Figure 3b. Simulated pressure time series at Tortoise in Figure 3d shows consistent amplitude and arrival time with the pressure data at Tortoise for the first Rayleigh wave packet at 40 s in the 1–3 Hz frequency band. We observe discrepancies between RW-atmos and SPECFEM2D-DG wavetrain shape and duration owing to the lateral velocity heterogeneity in the CVMH model, which is not present in the one-dimensional (1-D) model used by RW-atmos. Rapid lateral velocity variations lead to a more dispersed fundamental mode Rayleigh wave-train and more intra/inter-modal conversions (Brissaud et al., 2020). This arrival is strongly correlated to the higher-order mode arrival at the seismic stations traveling at 3.5 km/s.

We assessed the uniqueness of the pressure waveform at Tortoise by running additional simulations using various attenuation models (Graves & Pitarka, 2010; Olsen et al., 2003), seismic models (CVMS4.26 and CVMH, see supplementary Section S6.1), focal mechanisms (see supplementary Section S6.2) and topography models (see supplementary Section S6.3). The CVMH model, which includes a shallow sedimentary layer with shear velocities <1 km/s, provides the best fit and leads to larger amplitude of the first arrival, matching the duration and amplitude of the observed data, further supported by the strong site effects in the region (see Figure 2a). Our simulations using the CVMS4.26 model showed that the absence of a shallow waveguide leads to a dominant late arrival near 50s, not present in data, regardless of the attenuation model. Additionally, simulations introducing a deep low-velocity layer show larger duration and arrival time than observed in the data. The strong dependence of wavetrain envelopes on the velocity model further supports the choice of the CVMH velocity model, as it provides the best fit to observed signal characteristics.

4. Retrieving Rayleigh Wave Dispersion Properties Using Infrasound

The large correlations between vertical ground motion and pressure signals (see Figure 3e) allow for retrieval of subsurface velocities from the observed pressure dispersion characteristics. Figures 4a and 4c show a delay of 10s between the peak amplitude in the seismic data at RMM and in the acoustic data at Tortoise, consistent with the acoustic propagation time in the atmosphere. Single-component observations do not allow for traditional ellipticity measurements to invert for the velocity structure (Fäh et al., 2001). Yet, when the source location is known, the extraction of group velocity curves and identification of Rayleigh wave modes at the balloon can provide a first-order estimate of the average velocities and main discontinuities at

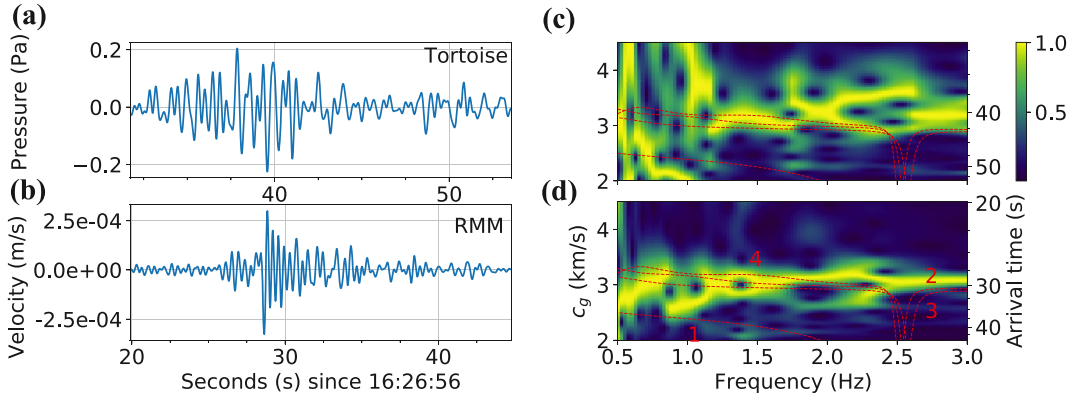

Figure 4. Frequency-Time ANalysis (FTAN) analysis of seismic and acoustic records. (a) Pressure time-series after event R1b at Tortoise, and (b) seismic vertical velocities at station RMM. (c), Corresponding FTAN group velocity between 0.2–3 Hz and 2–4.5 km/s of raw pressure data at Tortoise, and (d) of the seismic record for event R1b at station RMM. Arrival times corresponding to each group velocity value are shown on the right axis of plots (c) and (d). Theoretical group velocity curves computed at the epicenter using the CVMH model, which provides the best fit to data, are plotted in red over each panel for comparison. The red number over each curve indicates the mode number, with "1" corresponding to the fundamental mode.

depth. We performed a Frequency-Time ANalysis (FTAN, Levshin et al., 1972) of both acoustic and seismic signals (see supplementary Section S6.1) to determine the dispersion properties of the Rayleigh wave underneath the balloon. The FTAN decomposition consists of separating a highly dispersed signal into a number of short, narrow-band waves that arrive at different times to infer the frequency dependence of group velocity. The acoustic and seismic waveforms recorded at the balloon and at the seismic-station RMM are shown in Figure 4 along with their FTAN decomposition. The inferred group velocity curves do not clearly show the expected decreasing velocities with increasing frequencies. This is because each frequency is normalized independently and the seismic wavefield is composed of a mixture of interfering higher order modes. However, we observe strong correlations in the range of inferred group velocity values for frequencies >1 Hz corresponding to the detected arrival at Tortoise between 35 and 45 s after event R1b. Theoretical group velocity curves at the epicenter indicate that the higher order Rayleigh wave modes match the range and variations of group velocities highlighted by the FTAN analysis.

The identification of each Rayleigh wave mode provides constraints on the subsurface shear velocities since each mode shows different sensitivity with depth (Haney & Tsai, 2015). Green's functions-based inversion methods are used to build 1-D velocity models from dispersion data. Comparisons between data and theoretical group velocity curves in Figures 4c and 4d indicate that the waveform is dominated by the first three overtones in the 1–2.5 Hz frequency range. However, the low SNR and strong interference among higher order modes observed at Tortoise prevent accurate extraction of the variations of each mode with frequency, and therefore introduces large uncertainties during the inversion of Green's functions. Instead, we can simplify the inversion problem of building a full 1-D profile by determining only an estimate of the shear velocity at the depth of maximum sensitivity for an assumed dominant mode. The depth of maximum sensitivity of Rayleigh wave higher order modes can be empirically determined by (Haney & Tsai, 2015),

$$d(m,\lambda) = \frac{1}{2} m\lambda, \tag{1}$$

where d (km) is the depth of maximum sensitivity, $m > 0$ is the mode number, and λ (km) is the wavelength. From the group velocity range 2.7–3.3 km/s between 1 and 2.5 Hz highlighted by the FTAN analysis in Figure 4b, we can compute the dominant Rayleigh wavelengths. By considering that any of the first three overtones has equal probability to dominate the wavefield at a given frequency, we can compute the frequency-averaged depth at maximum-sensitivity in Equation 1, from all possible combinations of dominant modes $m \in \mathbf{M}$, $\mathbf{M}$ a list of N_m possible modes, and wavelengths $\lambda = (v_j \,/\, f_i)_{i,j=1:N_f,1:N_v}$, where

$(f_i)_{i=1:N_f}, (v_j)_{j=1:N_v}$ are the frequency and group velocity range, with N_f, N_v the number of discrete frequencies and group velocities included in the analysis, such that

$$d = \frac{1}{N_f}\sum_{i}^{N_f}\left\{\frac{1}{N_m N_v}\sum_{m\in\mathbf{M}}\sum_{j}^{N_v} d(m, v_j / f_i)\right\} \approx 2.4 \pm 0.6\text{km}. \quad (2)$$

Shear velocities between 2.7 and 3.3 km/s match the CVMH velocity range between 1.5 and 3 km depth (see supplementary Figure S51). The consistency between the shear velocity estimate determined through FTAN analysis and the values in the CVMH model suggests the possibility of using infrasound data to constrain the depths of shear velocity discontinuities in the subsurface.

The large uncertainty in shear velocity estimate highlights the need to: (a) accurately identify Rayleigh wave mode variations versus frequency, (b) constrain the source depth and characteristics, and (c) quantify the influence of topographic and lateral velocity variations on pressure waveform frequency dependence. Accurate identification of Rayleigh wave modes requires significant noise reduction in the pressure records and/or a clear separation between each mode's arrival time. For example, FTAN analyses of simulated waveforms show much less smeared outgroup velocity curves (see supplementary Section S6.1). We ran additional simulations for event R1b using a flat ground-air interface to assess the influence of different focal mechanisms (see supplementary Section S6.2), and topography and source effects (see supplementary Section S6.3). Numerical results with variations in focal mechanism indicate that reverse-fault and normal-fault sources lead to absolute pressure amplitudes up to five times larger than strike-slip sources, but the pressure signal envelopes show similar variations with time (see supplementary Section S6.2), suggesting that inferred dispersion properties provide more constraints on path rather than source effects. Finally, simulations with and without topography indicate that the relative strength of the second wave packet is greatly enhanced by the scattering and inter-modal conversions of body and surface waves traveling through the topography. Topographic variations are therefore crucial to account for when inverting for seismic velocities to converge to a unique solution when using the full Rayleigh wave train.

5. Conclusions and Discussion

A magnitude 4.2 strike-slip event was detected 78 km from the epicenter by a balloon at 4.8 km altitude, which is the first detection of its kind. The acoustic signal is characterized by a narrow-band energy peak (1–3 Hz) excited by a higher mode Rayleigh wave. The acoustic spectrogram correlates strongly with Rayleigh wave seismic records beneath the balloon. Further, our analysis showed how the spectral nature of the detected Rayleigh wave signature may be used in conjunction with candidate subsurface models to invert for the shear velocity structure. Numerical simulations using various velocity models further confirmed the strong dependence of the Rayleigh wave signal on the subsurface structure. However, since the inversion problem is poorly constrained, iterative probabilistic methods have to be employed to obtain a physically consistent solution and quantify the uncertainty owing to lateral velocity variations and mode misidentification (Beaty et al., 2002).

In the text above and in the supplementary material, we presented a detailed analysis of seismo-acoustic phenomenology as it relates to airborne infrasound monitoring and described a systematic methodology for identifying seismic arrivals. For our catalog of shallow high-frequency events, we found significant interactions between shallow velocity structure and topography. Low-frequency energy generated by large earthquakes (and venusquakes) is expected to be less sensitive to small-scale variations of topography and seismic velocities in the near surface. Since the high-frequency earthquakes we analyzed are predominantly strike slip, epicentral and Rayleigh wave-induced infrasound signals are generally characterized by low SNR ($\ll$2). Most refracted epicentral waves did not reach the sensors since the balloons remained in the acoustic shadow zone at regional distances. Some events were too deep for low-frequency acoustic energy to propagate isotropically from the source (Averbuch et al., 2020). In the far field, the presence of topography led to strong Rayleigh wave scattering from large topographic gradients at high frequency (Wang et al., 2015) and defocusing in the atmosphere at low frequency, drastically reducing the acoustic amplitudes at the balloon. Despite these challenges, a moderately weak earthquake of magnitude 4.2 was successfully detected.

While our Earth-analog experiments are primarily aimed at detecting seismic activity on Venus, the development of balloon-based infrasonic remote sensing also has applications on Earth. Agile and reconfigurable balloon-based infrasound monitoring networks that capitalize on the ability of balloons to loiter in a given region (Bellemare et al., 2020) can be used to augment ground-based infrasound stations for monitoring of infrasound from natural and anthropogenic sources. In addition, the acoustic wavefield from volcanic activity can be characterized in a dimension that is inaccessible to ground-based networks (Matoza et al., 2017).

Having demonstrated the detectability of seismic infrasound from natural earthquakes on a high-altitude balloon platform, we will adopt a two-pronged approach involving simulation studies and the collection of more Earth-based aerial seismo-acoustic data to advance this technique toward application on Venus. In the next two years, we will conduct balloon flight campaigns in high-seismicity areas within the continental United States, with the aim of collecting seismo-acoustic signals from several earthquakes possessing different source mechanisms (thrust and normal-faulting earthquakes) over areas with differing subsurface structures and topography and in varied atmospheric conditions. We will implement several improvements to these flight campaigns, including the use of multiple absolute microbarometers on each flight to determine the direction of arrival. Our infrasound simulation tools will also be expanded to perform seismo-acoustic simulation studies to generate candidate infrasound arrivals from a variety of seismic events on Venus, especially accounting for the chemical and thermodynamic differences between Earth and Venus that may result in dispersive propagation in the Venus cloud layer at the upper edge of the infrasound frequency band (Trahan & Petculescu, 2020).

The interpretation of pressure waveforms at the balloon relies heavily on prior determination of the source depth and location, which is a considerable technical challenge with a single sensor and needs constraints from external data. At the current stage of development, our methods rely on ground truth data generated by terrestrial seismic networks, and our future development is focused on the task of signal identification and inversion without ground-based data. The detection of acoustic waves generated by multiple seismic phases from the same event is of particular interest, as this would enable the inversion of the range of crustal velocities, and potentially the depth of the seismogenic layer, from a single balloon station. If additional sensors are present on the balloon or observations from multiple balloons available, the time delay between the arrivals will greatly improve signal interpretation.

The detection and characterization of earthquakes from a balloon through a combination of experiments and high-fidelity simulations holds the key for future seismology on Venus. Therefore, the first data point collected in this effort represents a significant milestone.

Appendix A: Data and Methods

All data and methods can be found in the supplementary material (see supplementary Section S1). The various subsections of the Supplementary describe specific aspects of the data and methodology:

- Section S1.1: description of the earthquake catalog and seismic data
- Section S1.2: description of the modeling tools, seismic and atmospheric background velocity models
- Section S1.3: description of the event-selection procedure used in Section 3

Data Availability Statement

Data Availability Seismic waveform data and earthquake catalogs were accessed through the Southern California Earthquake Data Center (SCEDC, https://scedc.caltech.edu/data/) at Caltech (Southern California Earthquake Center, 2013). The community velocity models are obtained through the UCVM software framework maintained by Southern California Earthquake Center (Small et al., 2017). Balloon microbarometer and simulation data are available on a publicly accessible FigShare repository with https://doi.org/10.6084/m9.figshare.14374067.

Acknowledgments
The authors acknowledge financial support from the Strategic Research and Technology Development and the Instantaneous and Spontaneous Concept grants at the Jet Propulsion Laboratory (JPL). Support from the NASA Planetary Science and Technology through Analog Research (PSTAR) program is also gratefully acknowledged. In addition, the authors would like to thank Noah Yared, Christine Yuan, Kyle Weng, Michael Lally, Luan Nguen, David Komjathy, Adam Komjathy, and Katalin Komjathy for their assistance in constructing Heliotrope envelopes. They thank Kirk Barrow and Chris Yahnker (JPL) for their help in recovering the balloons. Crescenta Valley High School in La Crescenta, CA is gratefully acknowledged for providing space for Heliotrope construction. The authors would like to thank Zachary Ross, Yan Yang, and Zhe Jia (Seismological Laboratory, California Institute of Technology) for insightful discussions regarding earthquake catalogs and the interpretation of regional seismic data. They also thank the W.M. Keck Institute for Space Studies for their early support of the balloon-based seismology project. Finally, they would like to thank the two reviewers for their detailed comments and suggestions for the manuscript. Part of this research was performed at the Jet Propulsion Laboratory, California Institute of Technology with support from internal research and development grants, under a contract with the National Aeronautics and Space Administration. Sandia National Laboratories is a multimission laboratory managed and operated by National Technology and Engineering Solutions of Sandia, LLC, a wholly owned subsidiary of Honeywell International, Inc., for the U.S. Department of Energy's National Nuclear Security Administration under Contract No. DENA0003525. The views expressed here do not necessarily reflect the views of the United States Government, the United States Department of Energy, or Sandia National Laboratories.

References

Anderson, J. F., Johnson, J. B., Bowman, D. C., & Ronan, T. J. (2018). The gem infrasound logger and custom-built instrumentation. *Seismological Research Letters*, *89*, 153–164. https://doi.org/10.1785/0220170067

Arrowsmith, S. J., Burlacu, R., Pankow, K., Stump, B., Stead, R., Whitaker, R., & Hayward, C. (2012). A seismoacoustic study of the 2011 January 3 Circleville earthquake. *Geophysical Journal International*, *189*, 1148–1158. https://doi.org/10.1111/j.1365-246X.2012.05420.x

Averbuch, G., Waxler, R. M., Smets, P. S. M., & Evers, L. G. (2020). Probabilistic inversion for submerged source depth and strength from infrasound observations. *Journal of the Acoustical Society of America*, *147*, 1066–1077. https://doi.org/10.1121/1.510175110.1121/10.0000695

Banister, J. R., & Hereford, W. V. (1991). Observed high-altitude pressure waves from an underground and a surface explosion. *Journal of Geophysical Research*, *96*, 5185–5193. https://doi.org/10.1029/90JD02640

Bass, H. E., Hetzer, C. H., & Raspet, R. (2007). On the speed of sound in the atmosphere as a function of altitude and frequency. *Journal of Geophysical Research*, *112*. https://doi.org/10.1029/2006JD007806

Beaty, K. S., Schmitt, D. R., & Sacchi, M. (2002). Simulated annealing inversion of multimode Rayleigh wave dispersion curves for geological structure. *Geophysical Journal International*, *151*(2), 622–631. https://doi.org/10.1046/j.1365-246x.2002.01809.x

Bellemare, M. G., Candido, S., Castro, P. S., Gong, J., Machado, M. C., Moitra, S., et al. (2020). Autonomous navigation of stratospheric balloons using reinforcement learning. *Nature*, *588*, 77–82. https://doi.org/10.1038/s41586-020-2939-8

Berg, E. M., Lin, F.-C., Allam, A., Qiu, H., Shen, W., & Ben-Zion, Y. (2018). Tomography of southern California via Bayesian joint inversion of Rayleigh wave ellipticity and phase velocity from ambient noise cross-correlations. *Journal of Geophysical Research: Solid Earth*, *123*, 9933–9949. https://doi.org/10.1029/2018jb016269

Blom, P., & Waxler, R. (2012). Impulse propagation in the nocturnal boundary layer: Analysis of the geometric component. *Journal of the Acoustical Society of America*, *131*, 3680–3690. https://doi.org/10.1121/1.3699174

Bowman, D. C., & Lees, J. M. (2017). A comparison of the ocean microbarom recorded on the ground and in the stratosphere. *Journal of Geophysical Research: Atmospheres*, *122*, 9773–9782. https://doi.org/10.1002/2017jd026474

Bowman, D. C., Norman, P. E., Pauken, M. T., Albert, S. A., Dexheimer, D., Yang, X., et al. (2020). Multihour stratospheric flights with the Heliotrope solar hot-air balloon. *Journal of Atmospheric and Oceanic Technology*, *37*, 1051–1066. https://doi.org/10.1175/JTECH-D-19-0175.1

Brissaud, Q., Bowden, D. C., & Tsai, V. C. (2020). Extension of the basin Rayleigh-wave amplification theory to include basin-edge effects. *Bulletin of the Seismological Society of America*, *110*, 1305–1322. https://doi.org/10.1785/0120190161

Brissaud, Q., Martin, R., Garcia, R. F., & Komatitsch, D. (2017). Hybrid Galerkin numerical modelling of elastodynamics and compressible Navier-Stokes couplings: Applications to seismo-gravito acoustic waves. *Geophysical Journal International*, *210*, 1047–1069. https://doi.org/10.1093/gji/ggx185

Byrne, P. K., Ghail, R. C., Ghail, R. C., Şengör, A. M. C., James, P. B., Klimczak, C., & Solomon, S. C. (2018). The globally fragmented, mobile lithosphere of Venus May resemble the permobile tectonic regime of Archean Earth. *GSA annual meeting in Indianapolis, Indiana, USA*. https://doi.org/10.1130/abs/2018am-323063

Chunchuzov, I., Kulichkov, S., Perepelkin, V., Popov, O., Firstov, P., Assink, J. D., & Marchetti, E. (2015). Study of the wind velocity-layered structure in the stratosphere, mesosphere, and lower thermosphere by using infrasound probing of the atmosphere. *Journal of Geophysical Research: Atmospheres*, *120*, 8828–8840. https://doi.org/10.1002/2015JD023276

Cutts, J. A., Matthies, L., & Thompson, T. W., & Aerial Platforms Study Team. (2018). *Aerial platforms for the scientific exploration of Venus (Tech. Rep.)*. NASA Jet Propulsion Laboratory/California Institute of Technology. 10.13140/RG.2.2.15808.89601

Didion, A., Cutts, J., Lognonne, P., Kenda, B., Drilleau, M., Makela, J., et al. (2018). Remote sensing of Venusian seismic activity with a small spacecraft, the VAMOS mission concept. In *2018 IEEE aerospace conference* (pp. 1–14). https://doi.org/10.1109/AERO.2018.8396447

Esposito, L. W. (1984). Sulfur dioxide: Episodic injection shows evidence for active Venus volcanism. *Science*, *223*, 1072–1074. https://doi.org/10.1126/science.223.4640.1072

Fäh, D., Kind, F., & Giardini, D. (2001). A theoretical investigation of average H/V ratios. *Geophysical Journal International*, *145*, 535–549. https://doi.org/10.1007/978-3-319-75295-2_610.1046/j.0956-540x.2001.01406.x

Fee, D., & Matoza, R. S. (2013). An overview of volcano infrasound: From Hawaiian to Plinian, local to global. *Journal of Volcanology and Geothermal Research*, *249*, 123–139. https://doi.org/10.1016/j.jvolgeores.2012.09.002

Filiberto, J., Trang, D., Treiman, A. H., & Gilmore, M. S. (2020). Present-day volcanism on Venus as evidenced from weathering rates of olivine. *Science Advances*, *6*, eaax7445. https://doi.org/10.1126/sciadv.aax7445

Garcia, R., Lognonné, P., & Bonnin, X. (2005). Detecting atmospheric perturbations produced by Venus quakes. *Geophysical Research Letters*, *32*. https://doi.org/10.1029/2005gl023558

Garcia, R. F., Martire, L., Chaigneau, Y., Cadu, A., Mimoun, D., Portus, M. B., et al. (2020). An active source seismo-acoustic experiment using tethered balloons to validate instrument concepts and modelling tools for atmospheric seismology. *Geophysical Journal International*, *225*, 186–199. https://doi.org/10.1093/gji/ggaa589

Gilmore, M. S., & Beauchamp, P. M. (2020). *Venus flagship mission decadal study final report (Tech. Rep.)*. JPL, Caltech. https://doi.org/10.5194/hess-2020-169-ac1

Graves, R. W., & Pitarka, A. (2010). Broadband ground-motion simulation using a hybrid approach. *Bulletin of the Seismological Society of America*, *100*, 2095–2123. https://doi.org/10.1785/0120100057

Gülcher, A. J. P., Gerya, T. V., Montési, L. G. J., & Munch, J. (2020). Corona structures driven by plume-lithosphere interactions and evidence for ongoing plume activity on Venus. *Nature Geoscience*, *13*, 547–554. https://doi.org/10.1038/s41561-020-0606-1

Haney, M. M., & Tsai, V. C. (2015). Nonperturbational surface-wave inversion: A dix-type relation for surface waves. *Geophysics*, *80*, EN167–EN177. https://doi.org/10.1190/geo2014-0612.1

Hernandez, B., Le Pichon, A., Vergoz, J., Herry, P., Ceranna, L., Pilger, C., et al. (2018). Estimating the ground-motion distribution of the 2016 Mw 6.2 Amatrice, Italy, earthquake using remote infrasound observations. *Seismological Research Letters*, *89*, 2227–2236. https://doi.org/10.1785/0220180103

Johnson, J. B., Mikesell, T. D., Anderson, J. F., & Liberty, L. M. (2020). Mapping the sources of proximal earthquake infrasound. *Geophysical Research Letters*, *47*, e2020GL091421. https://doi.org/10.1029/2020GL091421

Kanamori, H., & Mori, J. (1992). Harmonic excitation of mantle Rayleigh waves by the 1991 eruption of mount pinatubo, philippines. *Geophysical Research Letters*, *19*, 721–724. https://doi.org/10.1029/92GL00258

Kremic, T., & Hunter, G. W. (2019). Long-lived in-situ solar system explorer (LLISE). In *17th Venus exploration and analysis group (VEXAG) meeting*. Retrieved from https://ntrs.nasa.gov/citations/20190034042

Krishnamoorthy, S., Bowman, D. C., Komjathy, A., Pauken, M. T., & Cutts, J. A. (2020). Origin and mitigation of wind noise on balloon-borne infrasound microbarometers. *Journal of the Acoustical Society of America*, *148*, 2361–2370. https://doi.org/10.1121/10.0002356

Krishnamoorthy, S., Lai, V. H., Komjathy, A., Pauken, M. T., Cutts, J. A., Garcia, R. F., et al. (2019). Aerial seismology using balloon-based barometers. *IEEE Transactions on Geoscience and Remote Sensing*, *57*(12), 10191–10201. https://doi.org/10.1109/TGRS.2019.2931831

Krishnamoorthy, S., Komjathy, A., Pauken, M. T., Cutts, J. A., Garcia, R. F., Mimoun, D., et al. (2018). Detection of artificially generated seismic signals using balloon-borne infrasound sensors. *Geophysical Research Letters*, *45*, 3393–3403. https://doi.org/10.1002/2018GL077481

Lamb, O. D., De Angelis, S., Wall, R. J., Lamur, A., Varley, N. R., Reyes-Dávila, G., et al. (2017). Seismic and experimental insights into eruption precursors at Volcán de Colima. *Geophysical Research Letters*, *44*(12), 6092–6100. https://doi.org/10.1002/2017GL073350

Lamb, O. D., Lees, J. M., & Bowman, D. C. (2018). Detecting lightning infrasound using a high-altitude balloon. *Geophysical Research Letters*, *45*, 7176–7183. https://doi.org/10.1029/2018gl078401

Levshin, A. L., Pisarenko, V. F., & Pogrebinsky, G. A. (1972). On a frequency-time analysis of oscillations. *Annales de Geophysique*, *28*, 211–218. https://doi.org/10.1111/j.1365-246x.1990.tb01786.x

Linkin, V. M., Kerzhanovich, V. V., Lipatov, A. N., Shurupov, A. A., Seiff, A., Ragent, B., et al. (1986). Thermal structure of the Venus atmosphere in the middle cloud layer. *Science*, *231*, 1420–1422. https://doi.org/10.1126/science.231.4744.1420

Lognonné, P., & Johnson, C. L. (2015). Planetary seismology. In G. Schubert (Ed.), *Treatise on geophysics* (2nd ed., pp. 65–120). Oxford: Elsevier. https://doi.org/10.1016/B978-0-444-53802-4.00167-6

Martire, L., Brissaud, Q., Lai, V. H., Garcia, R. F., Martin, R., Krishnamoorthy, S., et al. (2018). Numerical simulation of the atmospheric signature of artificial and natural seismic events. *Geophysical Research Letters*, *45*, 12085–12093. https://doi.org/10.1029/2018gl080485

Matoza, R. S., Jolly, A., Fee, D., Johnson, R., Chouet, B., Dawson, P., et al. (2017). Seismo-acoustic wavefield of strombolian explosions at Yasur volcano, Vanuatu, using a broadband seismo-acoustic network, infrasound arrays, and infrasonic sensors on tethered balloons. *Journal of the Acoustical Society of America*, *141*. https://doi.org/10.1121/1.4987573

Olsen, K. B., Day, S. M., & Bradley, C. R. (2003). Estimation of Q for long-period (>2 sec) waves in the Los Angeles Basin. *Bulletin of the Seismological Society of America*, *93*, 627–638. https://doi.org/10.1785/0120020135

Peebles, C. (1997). *High frontier: The U. S. air force and the military space program*. U. S. Government Printing Office.

Perevalova, N. P., Sankov, V. A., Astafyeva, E. I., & Zhupityaeva, A. S. (2014). Threshold magnitude for ionospheric TEC response to earthquakes. *Journal of Atmospheric and Solar-Terrestrial Physics*, *108*, 77–90. https://doi.org/10.1016/j.jastp.2013.12.014

Ross, Z. E., Idini, B., Jia, Z., Stephenson, O. L., Zhong, M., Wang, X., et al. (2019). Hierarchical interlocked orthogonal faulting in the 2019 ridgecrest earthquake sequence. *Science*, *366*, 346–351. https://doi.org/10.1126/science.aaz0109

Sagdeev, R. Z., Linkin, V. M., Kerzhanovich, V. V., Lipatov, A. N., Shurupov, A. A., Blamont, J. E., et al. (1986). Overview of VEGA Venus balloon in situ meteorological measurements. *Science*, *231*, 1411–1414. https://doi.org/10.1126/science.231.4744.1411

Shani-Kadmiel, S., Averbuch, G., Smets, P., Assink, J., & Evers, L. (2021). The 2010 Haiti earthquake revisited: An acoustic intensity map from remote atmospheric infrasound observations. *Earth and Planetary Science Letters*, *560*, 116795. https://doi.org/10.1016/j.epsl.2021.116795

Small, P., Gill, D., Maechling, P. J., Taborda, R., Callaghan, S., Jordan, T. H., et al. (2017). The SCEC unified community velocity model software framework. *Seismological Research Letters*, *88*, 1539–1552. https://doi.org/10.1785/0220170082

Smrekar, S. E., Stofan, E. R., Mueller, N., Treiman, A., Elkins-Tanton, L., Helbert, J., et al. (2010). Recent hotspot volcanism on Venus from VIRTIS emissivity data. *Science*, *328*, 605–608. https://doi.org/10.1126/science.1186785

Southern California Earthquake Center. (2013). *Caltech dataset*. https://doi.org/10.7909/C3WD3xH1

Stevenson, D. J., Cutts, J. A., Mimoun, D., Arrowsmith, S., Banerdt, W. B., Blom, P., et al. (2015). *Probing the interior structure of Venus (tech. Rep.)*. Keck Institute for Space Studies. https://doi.org/10.26206/C1CX-EV12

Trahan, A. J., & Petculescu, A. (2020). Absorption of infrasound in the lower and middle clouds of Venus. *Journal of the Acoustical Society of America*, *148*, 141–152. https://doi.org/10.1121/10.0001520

Wang, L., Xu, Y., Xia, J., & Luo, Y. (2015). Effect of near-surface topography on high-frequency Rayleigh-wave propagation. *Journal of Applied Geophysics*, *116*, 93–103. https://doi.org/10.1016/j.jappgeo.2015.02.028

Wescott, J. W. (1965). Acoustic detection of high-altitude turbulence. In *AFCRL scientific balloon symposium*. Retrieved from https://apps.dtic.mil/sti/citations/AD0434705

Wood, A. T., Wattson, R. B., & Pollack, J. B. (1968). Venus: Estimates of the surface temperature and pressure from radio and radar measurements. *Science*, *162*, 114–116. https://doi.org/10.1126/science.162.3849.114